Editors' Suggestion | Featured in Physics

Hydrodynamic Elastocapillary Morphing of Hair Bundles

Jonghyun Ha,[1] Yun Seong Kim,[1] Kaiying Jiang,[1] Ryan Siu,[1] and Sameh Tawfick[1,2,*]
[1]Department of Mechanical Science and Engineering, University of Illinois at Urbana-Champaign, Urbana, Illinois 61801, USA
[2]The Beckman Institute for Advanced Science and Technology, University of Illinois at Urbana-Champaign, Urbana, Illinois 61801, USA

(Received 18 March 2020; revised 30 June 2020; accepted 11 November 2020; published 16 December 2020; corrected 13 January 2021)

We report polymorphic self-assembly of hair arranged in hollow bundles driven by capillarity, hydrodynamics, and elasticity. Bundles emerging from a liquid bath shrink but remain hollow at slow drainage due to the negative pressure of the menisci trapped between the hairs. The timescale allows the collective stiffening of the fibers to resist closure. At fast drainage, the bundles fully close before the liquid can drain through the hair. A liquid column trapped in the hole closes the bundle while the lubricated hairs still behave softly. Scaling laws predict this reversible hair polymorphism.

DOI: 10.1103/PhysRevLett.125.254503

Very long aspect ratio hairs in liquid exhibit intriguing synchronized motion and self-assembly. For instance, the functionality of biological cilia is enabled by their synchronized beating, large elastic deformation, and constant rearrangement [1]. At the nanoscale, carbon nanotubes self-assemble into curious patterns during drying [2,3]. These unusual patterns are observed when large numbers of dense hairs rearrange due to capillarity. These beautiful phenomena have induced scientists to study elastocapillarity, where capillary pressure readily deforms soft slender materials [4–6], and liquid rise in soft solids [7,8]. Recently, interesting new phenomena were observed when self-assembly of soft hair is driven at higher rates, leading to polymorphic self-assembly related to hydrodynamics [9–11]. The rich solid-liquid phenomena at the transition from static capillarity to hydrodynamics are unexplored, and, more importantly, the understanding of the timescale of the transition from slow aggregation to synchronous beatinglike motion is absent.

Here, we study the self-assembly of wet hair that exhibits rate-dependent self-assembly [9,10] to understand the transition from static capillarity to hydrodynamic polymorphism. Hairlike carbon fibers are assembled perpendicular to a base having a ring-shaped cross section, forming a hollow bundle that we refer to as a "hairy-wall tube," which differs from a regular hair bundle by having an inner hole [Fig. 1(a) and Movie S1 in Supplemental Material [12]]. Hair is immersed in a liquid container, and, depending on the bundle's diameter, height, and the drain rates as they pierce the liquid-to-air interface, we observe two distinct deformation modes of the hollow bundles. Bundle shrinkage without hole closure is observed for short bundles and slow rates, while a single radial beat leading to complete closure occurs for long bundles and at fast rates. We had previously observed capillary-induced twisting of hairs for softer bundles having a smaller number of hairs and at high speeds [10]. In the current study, we investigate a larger range of drain rates and bundle geometries to explore the various deformation modes as a function of hair length,

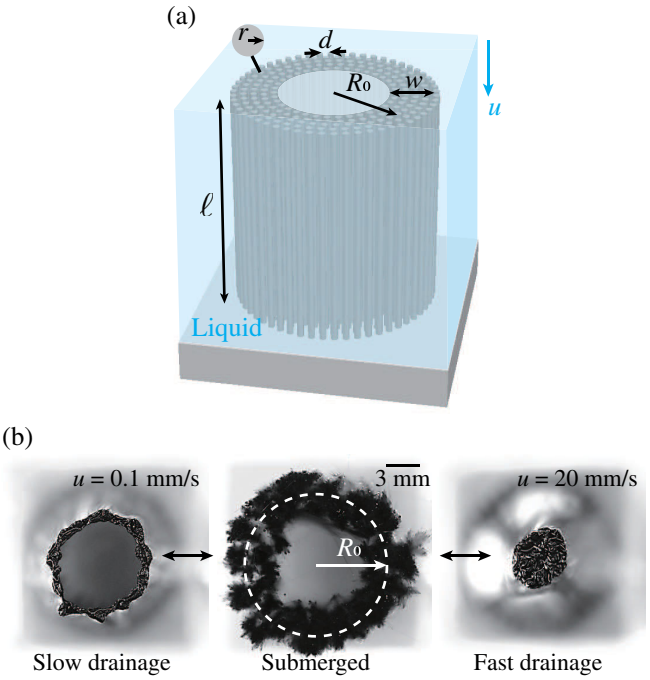

FIG. 1. Hydrodynamic elastocapillarity-induced polymorphism of hairy tubes. (a) Schematics of hairy tubes. R_0, w, r, d, and ℓ correspond to the inner radius, the thickness of the tubes, fiber radius, spacing, and length, respectively. (b) Top views of the hairy tubes ($R_0 = 7$ mm, $\ell = 25$ mm). The middle image indicates the shape of the initial state. The left and right images indicate the final shape of the partial closure (slow drainage, $u = 0.1$ mm/s) and the complete closure (fast drainage, $u = 20$ mm/s), respectively.

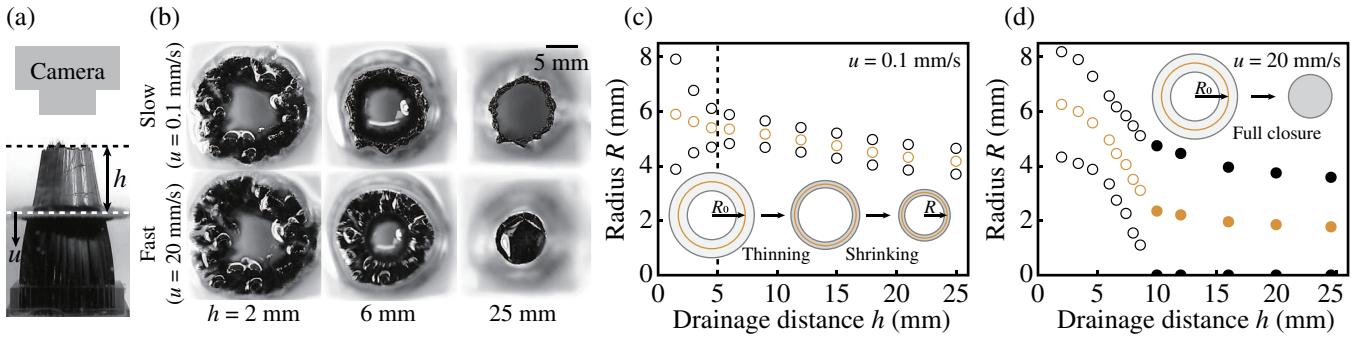

FIG. 2. Evolution of tube closure. (a) Side view of hairy tubes ($R_0 = 7$ mm, $\ell = 25$ mm). The ring-shaped images are captured by a top camera. (b) Drainage distance evaluation of tube closure. Top and bottom images correspond to slow ($u = 0.1$ mm/s) and fast drainage ($u = 20$ mm/s), respectively. h and R correspond to the drainage distance and the contracted radius, respectively. Movie S1 [12] shows the reversibility between partial and complete closure. (c) Fiber densification and shrinking regimes of partial closure at slow drainage. The left side from the dashed line indicates fiber densification, and the right side indicates shrinking (partial closure). (d) Diameter evolution during complete closure at fast drainage. Empty and filled symbols correspond to the partial and complete closure, respectively. Orange circle markers correspond to the average radius between outer and inner radii. Upper and lower black circle markers correspond to the outer and inner radius, respectively.

organization, liquid properties, and drain dynamics (see S1 in Ref. [12]). The coupling between capillarity, hydrodynamics, and elasticity leading to polymorphism has implications on other areas of physics and materials.

We fabricate the hairy tube by inserting carbon fiber bundles into a circular hole pattern on a base (see S2 in Ref. [12]). Then, we submerge the hairy tubes and then push the base out of the water using a motorized linear stage (EAS series, Orientalmotor), as shown in Fig. 1(a). The drainage velocity u is defined as the set speed of the linear stage. The middle image in Fig. 1(b) shows the top view of the immersed hairy tubes with length ℓ and hole radius R_0. Once the tubes pierce the water interface, fibers assemble due to surface tension. The pattern selection is set by ℓ, R_0, and u. The same hair bundle morphs from one geometry to another as a function of u. For short bundles and especially in the slow-drainage regime (low u), the holes shrink but resist full closure: The hair organization remains as hollow tubes with dense hairs at the wall, as shown in the left image in Fig. 1(b). We refer to this shrinkage as partial closure. However, the holes completely close at fast drainage (high u), as shown in the right image in Fig. 1(b). Therefore, the interaction of bundle geometry (elastocapillarity) and drainage hydrodynamics determines the morphology of assembled hairs.

To explain this morphing phenomenon, we get insights by tracking the kinematics of hole closure to plot the mean radius of the bundle, R, as we increase the drainage distance h, during the lowering of the water interface. Figure 2(a) shows the experimental setup. The evolution of R is quite different between the two cases, i.e., slow and fast drainage. During slow drain, the hairs locally coalesce first, and the tube wall thins before the mean diameter starts shrinking as shown in the top images in Fig. 2(b). Initially, the outer radius of the tube contracts while the inner radius increases [see Fig. 2(c)]. In the later stage, both outer and inner radii of the tubes shrink. Interestingly, in the fast-drainage conditions, the order of the two stages flips: We observe hole closure where the fibers move inward in a synchronized fashion before wall thinning. The hairs also appear fully submerged during the initial hole closure at fast drain rate as shown in the bottom images in Fig. 2(b) and the plot in Fig. 2(d).

We schematically plot our understanding of the slow-drainage mechanism in Fig. 3(a). This assembly is governed by balance between capillary forces in the small menisci between fibers and the collective stiffening of the dense fibers. The densification and fiber rearrangement are critical to take into consideration to understand the resistance of the bundle to full closure in the slow regime. By considering the surface energy of annular bundles, we show that the tangential (hoop) force F_c can be written as $F_c \sim \gamma h$, where γ is the surface tension (see S3 in Ref. [12] and also Ref. [13]). This force also results from the long meniscus trapped between dense fibers in circular arrangement, and the relation captures the intuitive increase in F_c with the increase in the meniscus height h as the liquid is drained [Fig. 3(a)]. We note that the contact angle between the fibers and the liquid is 20°. The elastic resistance results not only from the simple bending of individual hairs, but also from the contact resistance and hair rearrangement during slow drainage. We consider a fibrous array where the fibers sequentially contact each other, and their resistance increases as they densify. In this dense case, the elastic force is $F_e \propto \delta^2$, where δ is the hair deflection as they come in contact during the radial shrinkage of the hollow bundle (see S3 in Ref. [12]). In particular, as δ increases, the thickness of the tube walls will increase, leading to packing into a dense arch. The packing of the fibers effectively leads to higher resistance to capillary compression. By taking account of the reorganization of hair in the hollow bundle and the packing effects, we can get the final form of the elastic tangential

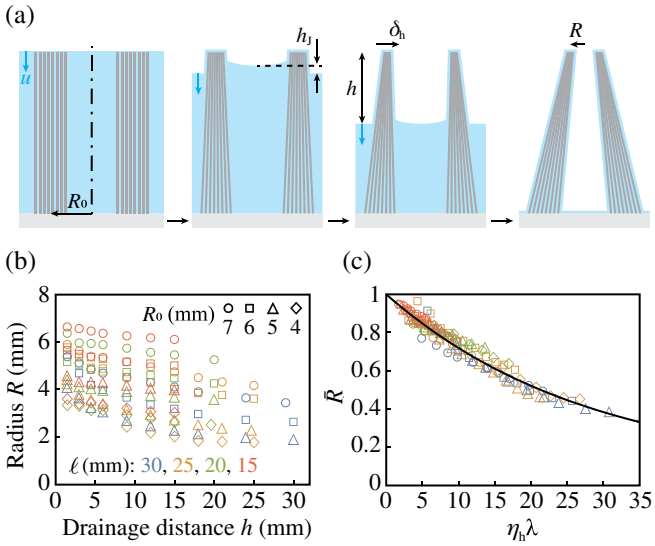

FIG. 3. Capillarity-driven partial closure at slow drainage. (a) Schematics of a side view of slow-drainage mechanism. The drainage process goes from left to right. (b) Experimentally measured tube radii versus drainage distance for various bundle geometries. (c) Nondimensional $\bar{R}$ versus drainage distance $\eta_h\lambda$, where λ is the aspect ratio. The experimental data collapse onto a single line when plotted against our scaling law, Eq. (1).

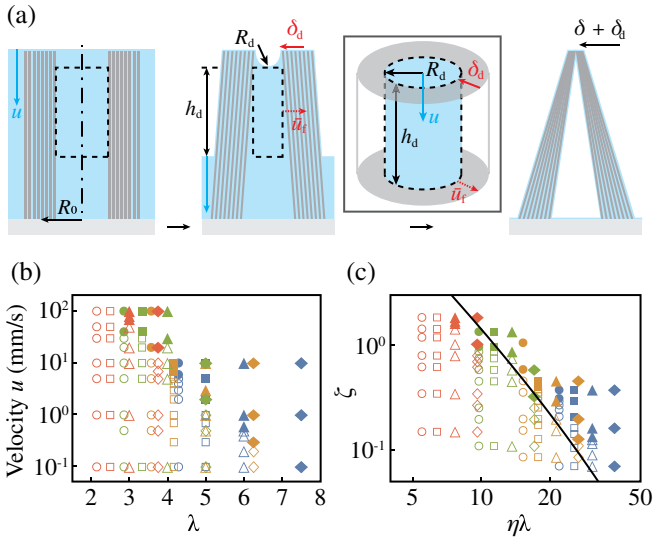

FIG. 4. Hydrodynamic-driven full closure at fast drainage. (a) Schematics of a side view of fast-drainage mechanism. The black box corresponds to the control volume of mass conservation. The drainage process goes from left to right. (b) Regime map of hair morphing where λ is the aspect ratio. Empty and filled symbols correspond to the partial and complete closure, respectively. (c) Universal regime map where ζ is the dimensionless dynamic rise and $\eta\lambda$ is the dimensionless drainage height with respect to ℓ_{ec}. The black line corresponds to the transition from partial to complete closure according to the theoretical model, Eq. (3). According to the theoretical line, the lower and upper regions indicate partial and complete closure, respectively. The markers for different geometries are listed in Fig. 3(b).

$F_e \sim \alpha EIR_0\delta^2/[r\ell^3(R_0-\delta)]$, where E and I are the Young's modulus and second moment of area of a single fiber, respectively (see S3 in Ref. [12]). The structural coefficient α can be written as $\alpha = \alpha_p w\rho_0/(r\rho_f)$, where ρ_0 and ρ_f are the fiber area fraction of the top surface in the initial and final shape, respectively (see S3 in Ref. [12]). α_p is a prefactor. Please note that F_e is dependent on stiffening and rearrangement, and, without this added complexity, the model would incorrectly predict full closure at any drain rate. We parametrize $\delta_h = \delta(h)$ to analyze the kinematics of the slow drainage as a function of the quasistatic drain height.

The force balance $F_c \sim F_e$ leads to $\gamma h \sim \alpha EIR_0\delta_h^2/[r\ell^3(R_0-\delta_h)]$. Noting the relation between the circumferential and radial deflections, we define $\bar{\delta}_h = \delta_h/R_0$ as the dimensionless radial deflection, $\eta_h = (h\ell)^{1/2}/\ell_{ec}$ as a kinematic elastocapillary number, and $\lambda = \ell/R_0$ as the aspect ratio of the hollow tubes. The length $\ell_{ec} = [EI/(r\gamma)]^{1/2}$ is the elastocapillary length balancing the surface tension and the stiffness of a fiber [4]. The dimensionless force balance reads $(\eta_h\lambda)^2 \sim \alpha\bar{\delta}_h{}^2/(1-\bar{\delta}_h)$, showing the scaling between the elastocapillarity of the hollow bundle (left) and the shrinkage (right). By solving a quadratic equation of $\bar{\delta}_h$, we obtain

$$\bar{\delta}_h \sim \frac{[(\eta_h\lambda)^4 + 4\alpha(\eta_h\lambda)^2]^{1/2} - (\eta_h\lambda)^2}{2\alpha}, \qquad (1)$$

describing the shrinkage not only as a function of the length, but also the instantaneous drainage height through the use of η_h. To corroborate the kinematic model, we normalize the measured $R(=R_0-\delta_h)$ by R_0, which leads to the nondimensional contracted radius $\bar{R} = 1-\bar{\delta}_h$ in Fig. 3(b) according to our scaling law [Eq. (1)] in Fig. 3(c). We observe that the experimental data for various tube geometries (see S1 in Ref. [12]) are collapsed onto a single master curve despite the various number of fibers, consistent with our theory. This result highlights that, for slow drain rates, the self-assembly is governed by static elastocapillarity, where fiber densification and stiffening due to rearrangement play a critical role in determining the final morphology.

The hollow bundle fully collapses (hole closure) at fast drainage, as shown in Fig. 4 and Movie S1 [12]. Figure 4(b) shows the hole closure regime map by experimentally varying the drain speed and geometry of the bundles. Qualitatively, during fast drainage, a long liquid column, $h_d \gg h_J$ [see Figs. 3(a) and 4(a)], is trapped in the bundle during the drainage and causes the full closure. This column is governed by viscous dissipation, which takes place at the fiber spacing d. The liquid drainage through the fiber spacings is restricted due to large viscous stresses within the narrow d, trapping a tall column in the bundle hole. The negative capillary pressure within this dynamic rise pulls the soft wall, causing it to completely close.

The competition between the timescales of fiber aggregation (bundle wall thinning) τ_a and inner diameter closure (flopping) τ sets the transition between slow and fast drainage (see S4 in Ref. [12]). At slow drainage, where the viscous dissipation can be neglected, fiber aggregation precedes inner diameter closure $\tau_a < \tau$ versus $\tau < \tau_a$ at a fast drain rate.

A scaling law governs the formation of a tall liquid column within the inner hole of the tube, leading to complete closure, as schematically shown in Fig. 4(a). Calculating h_d as a function of drain velocity u can be used for the scaling of the dynamic capillary force f_c. The bundles behave very softly, so the radius of the liquid meniscus on the top of the tube, R_d, is formed obeying Jurin's law $h_d \sim \gamma/(\rho g R_d)$, where ρ and g are liquid density and the gravitational acceleration, respectively [14]. Along h_d, R_d generates negative pressure (see S5 in Ref. [12]). The timescale is set when the negative pressure pulls the bundle wall inward, generating a relative liquid flow in the outward direction. Considering viscous resistance ($\sim \mu \bar{u}_f w$) and compression ($\sim \Delta p d^2$) at a single pore, we can express the relative velocity $\bar{u}_f \sim (d^2/\mu)\Delta p/w$, where d is the length scale of the fluid conduit (fiber spacing). The pressure difference Δp is induced by capillarity and can be scaled as γ/R_d. Thus, $\bar{u}_f \sim (d^2/\mu)(\gamma/R_d)/w$. Applying mass conservation between vertical and radial flow, the relative radial flow rate can be expressed as $Q_f \sim \bar{u}_f h_d R_d$, and the flow rate of the liquid column in the vertical direction is $Q_h \sim u R_d^2$, when it reaches the steady state. Considering the continuity of the flows in vertical and radial directions, $Q_f = Q_h$, we get $h_d \sim u R_d/\bar{u}_f$. By using the relation $\bar{u}_f$ and $R_d \sim \gamma/(\rho g h_d)$, we finally express $h_d \sim [\gamma \mu w u/(\rho g d)^2]^{1/3}$.

Using h_d, we write the dynamic capillary force as $f_c \sim \Delta p A_d$. The capillary pressure within the column, $\Delta p \sim \gamma/R_d$, leads to the complete closure of the hollow bundle at fast drainage. The surface area of the liquid column in the tube scales as $A_d \sim R_d h_d$. Thus, the dynamical compression force can be written as $f_c \sim \gamma h_d$. Because the hairs do not have time to densify, they behave as a soft noninteracting structure before the tube wall thinning, as opposed to their collective stiffening in the slow-drainage rate. We can express $f_e \sim \beta R_0 E I \delta_d/(r\ell^3)$, where δ_d is the dynamical deflection and $\beta = \beta_p w \rho_0/r$ is a structural coefficient of noncoalesced fibers (see S6 in Ref. [12]). β_p is a prefactor. Normalizing the force balance, $f_c \sim f_e$, leads to $\gamma h_d \sim \beta R_0 E I \delta_d/(r\ell^3)$ and divided by R_0 provides

$$\bar{\delta}_d \sim (\eta\lambda)^2 \zeta \beta^{-1}, \tag{2}$$

where $\bar{\delta}_d = \delta_d/R_0$ is dimensionless deflection due to dynamic effects and $\eta = \ell/\ell_{ec}$ is the elastocapillary number. We note that η_h becomes η when h reaches ℓ. Parameter $\zeta = h_d/\ell$, governed by u, is the dimensionless dynamical rise height. We found that both the static and dynamic compression forces play a role in bundle closure. When the water base is below the fiber base (h reaches ℓ), the tubes undergo further deformation $\bar{\delta}$, related to capillary-induced fiber aggregation. We express $\bar{\delta}$ by replacing η_h in Eq. (1) with η. The nondimensional contracted radius of the final shape can be written as $\bar{R} = 1 - (\bar{\delta} + \bar{\delta}_d)$. When $\bar{R} = 0$, the tubes completely close, as shown in Fig. 4(a). Combining the relation $\bar{\delta}$ and Eq. (2), we can provide the scaling law of the complete closure:

$$\zeta \sim \frac{\beta}{(\eta\lambda)^2}(1 - \bar{\delta}), \tag{3}$$

where $\bar{\delta}$ is computed from Eq. (1) by replacing h with ℓ. The scaling law of Eq. (3) involves the dynamic rise effects (ζ), capillary-driven deformation effects (η), and the bundle geometry (λ). This is used to transform the regime map in Fig. 4(b) into the universal scaling law in Fig. 4(c). The hairy tubes completely close at high λ and u, which correspond to long ℓ (large flexibility) and small R_0. Even when the magnitude of the total deflection is small, it is enough to collapse the tubes with relatively small R_0. The drain dynamics set the collective stiffness of the bundle, making it behave softly or stiffly at fast and slow u, respectively. The equation $\bar{R} = 1 - \Omega$, where $\Omega = \bar{\delta} + \bar{\delta}_d$, is the dimensionless total deflection. The black curve in Fig. 4(c) is obtained when $\bar{\delta} + \bar{\delta}_d = 1$ and marks the transition between partial and complete closure (see S7 in Ref. [12]). In the region of $\zeta > 1$, where u is very fast, and small $\eta\lambda$, the scaling law has minor disagreements with the experiments. On the other hand, we confirm that these laws predict the behavior of, for instance, liquids with much higher viscosity (see S8 in Ref. [12]).

We have presented an experimental system to study fluid-structure interactions of dense flexible structures, exhibiting clear transition from static-capillarity-driven to hydrodynamic-driven assembly. This leads to polymorphism from open (annular) to closed bundles based on the drain rate. The phenomenon also manifests itself in other complex patterns such as triangular and multihole bundles (see S9 and Movie S2 in Ref. [12]). In particular, we find that the hairs collectively stiffen at slow drain rates to shrink without collapse, but, at faster rates, the liquid is trapped within the hole in the bundle and within the wall, leading to a soft behavior and full closure. We developed universal scaling laws to predict the kinematics of hole shrinkage during slow drainage and the transition from partial or complete closure, and these laws work for various liquid viscosities. We anticipate the current work to pave the way for developing reconfigurable shape-shifting systems which are actuated via capillarity, such as artificial muscles [15], soft robotics, and smart textiles.

This work was supported by AFOSR Young Investigator Program (Grant No. FA9550-19-1-0010), NSF CMMI (Grant No. 1825758), and National Research Foundation of Korea (Grant No. 2019R1A6A3A03032230).

*tawfick@illinois.edu

[1] A. Vilfan and F. Jülicher, Hydrodynamic Flow Patterns and Synchronization of Beating Cilia, Phys. Rev. Lett. **96**, 058102 (2006).
[2] S. Tawfick, J. Bico, and S. Barcelo, Three-dimensional lithography by elasto-capillary engineering of filamentary materials, MRS Bull. **41**, 108 (2016).
[3] M. Volder, S. Tawfick, S. J. Park, D. Copic, Z. Zhao, W. Lu, and A. Hart, Diverse 3D microarchitectures made by capillary forming of carbon nanotubes, Adv. Mater. **22**, 4384 (2010).
[4] A. Cohen and L. Mahadevan, Kinks, rings, and rackets in filamentous structures, Proc. Natl. Acad. Sci. U.S.A. **100**, 12141 (2003).
[5] J. Bico, B. Roman, L. Moulin, and A, Boudaoud, Elastocapillary coalescence in wet hair, Nature (London) **432**, 690 (2004).
[6] H.-Y. Kim and L. Mahadevan, Capillary rise between elastic sheets, J. Fluid Mech. **548**, 141 (2006).
[7] C. Duprat, J. Aristoff, and H. A. Stone, Dynamics of elastocapillary rise, J. Fluid Mech. **679**, 641 (2011).
[8] J. Ha and H.-Y. Kim, Capillarity in soft porous solids, Annu. Rev. Fluid Mech. **52**, 263 (2020).
[9] D. Shin and S. Tawfick, Polymorphic elastocapillarity: Kinetically reconfigurable self-assembly of hair bundles by varying the drain rate, Langmuir **34**, 6231 (2018).
[10] L. Kovanko and S. Tawfick, Capillary-induced hair twist, Langmuir **35**, 13421 (2019).
[11] A. Hadjittofis, J. R. Lister, K. Singh, and D. Vella, Evaporation effects in elastocapillary aggregation, J. Fluid Mech. **792**, 168 (2016).
[12] See Supplemental Material at http://link.aps.org/supplemental/10.1103/PhysRevLett.125.254503 for includes details of samples preparations, theoretical derivations, and "additional experimental results."
[13] J. Bico and D. Quéré, Rise of liquids and bubbles in angular capillary tubes, J. Colloid Interface Sci. **247**, 162 (2002).
[14] J. Jurin, An account of some experiments shown before the Royal Society; with an enquiry into the cause of the ascent and suspension of water in capillary tubes, Phil. Trans. R. Soc. London **30**, 739 (1718).
[15] P. Chen, Y. Xu, S. He, X. Sun, S. Pan, J. Deng, D. Chen, and H. Peng, Hierarchically arranged helical fibre actuators driven by solvents and vapours, Nat. Nanotechnol. **10**, 1077 (2015).

Correction: The name of the second author in Ref. [13] was processed improperly during the prepublication stage and has been fixed.

Supplementary Material for "Hydrodynamic elastocapillary morphing of hair bundles"

by Jonghyun Ha, Yun Seong Kim, Kaiying Jiang, Ryan Siu, and Sameh Tawfick

S1. Twisting behavior

In addition to partial and complete closures, we can observe the twisting behavior on hairy tubes. However, the twisting behavior appears only within a more limited range of drain speed and bundle geometry. The drain speed range u of the previous study [10] is 6.2 – 117 mm/s, while that of the current one is 0.1 – 100 mm/s, so the current study reaches a lower range of speeds which allow the detailed study of partial closure. In the previous study [10], $N = 138000$, while $N = 230000$ – 400200 (varied with the hole radius R_0) in the current work, indicating that the bundles in the present study are generally stiffer than the twisting study. According to our model, the stiffness of the bundles is proportional to the total number of fibers N, so the increase of N leads to the partial closure, and more resistant to twisting. In our previous twisting study, we have observed two modes of twisting having distinct kinematics [10]: (i) twisting after closure at intermediate speeds; and (ii) twisting during closure at the highest drain speeds. We have not observed type (i) twisting in this current study, probably due to the thicker wall geometry of the bundles. We have only observed two instances of type (ii) twisting out of all the experiments in this study. These two instances were observed at the tallest aspect ratio bundle and highest drain rate. We consider these two experiments to be in the full closure regime since concurrent tube closure is observed during twisting

S2. Fabrication of hairy bundles

To fabricate these hairy tubes, we insert carbon fiber tows (yarns of straight fibers) with length ℓ into a circular hole pattern on a base produced by a 3D printer (Micro Plus cDLM, Envisiontec). The depth of the holes goes throughout the base, and the hairs are fixed on the back using an adhesive tape. A single carbon fiber tow is approximately 0.25 mm radius and has approximately 4600 fibers each having radius r of 2.5 μm. When we submerge the hairy tubes, the tows homogeneously spread and fill the space of the hollow tube's wall. This allows us to assume that the tubes have the uniform spacing d between the fibers, as shown in Fig. S2. In the theoretical analysis, we are mainly interested two typical spacings: d and R_0. In addition to optical imaging, we have previously confirmed by X-ray tomography that the carbon fiber tows are indistinguishable after capillary assembly [9]. The spacing between the hair d varies during self-assembly due to coalescence, as well

as the inner radius R_0 of the hollow hair assembly as shown in Fig. 1(a). In the experiment, we use various geometries with different R_0 ranging from 4 to 7 mm and ℓ ranging from 15 to 30 mm, but constant thickness of the tubes, $w = 3$ mm consisting of three concentric circles.

S3. Kinematic models of the contracted radius in the slow drainage

S3.1. Compression force due to the surface energy of hollow bundles

We analyze the self-assembly by considering the capillary force on a single fiber due to the menisci trapped between it and the fibers next to it F_c. This simple analysis provides an insight into the complex behavior of the hair bundle, as evidenced by the agreement with experiments. We use energy arguments to express the capillary hoop compression force F_c during slow drainage. Here, we consider the stage where the fibers have already coalesced since the time scale of the fiber aggregation is smaller than that of the inner diameter closure: $\tau_\mathrm{a} < \tau$ (described in S3), so that the top area of the bundles A_r (ring area) is constant. The spacing between the fibers is smaller than their radii $d \sim r$. As the liquid surface is lowered by h, the tube shrinks by $\mathrm{d}\delta = R_0 - R$. Note that in the experiments, there are several circular rows of fibers and they re-arrange while they remain packed to accommodate the diameter shrinkage while keeping the packing almost constant. Figure S3 shows the tube shape change from state 1 to 2. We use the assumption that the bundle's wall thickness is small compared to the mean bundle radius for energy calculations. The surface area of the state 1 is $A_1 \sim A_\mathrm{r} + h\psi_0$, and that of the state 2 is $A_2 \sim A_\mathrm{r} + h\psi$ if $\mathrm{d}\delta \ll \ell$. We express the surface energy difference $\mathrm{d}E \sim \gamma \mathrm{d}A$, where $\mathrm{d}A$ is the surface area difference between the state 2 and 1, so $\mathrm{d}E \sim -\gamma h \mathrm{d}\psi$, where $\mathrm{d}\psi = \psi_0 - \psi$. The derivative of energy can give the capillary hoop compression force $F_\mathrm{c} = -\mathrm{d}E/\mathrm{d}\psi$, which results in $F_\mathrm{c} \sim \gamma h$.

The capillary hoop compression force F_c can also be obtained using simple force balance arguments. The tangential hoop force on a fiber sitting in the circumference of a hollow bundle is $F_\mathrm{c} \sim \Delta p A_\mathrm{s} \sim \gamma/a(hr)$, where Δp is the negative pressure in the meniscus between two fibers, A_s is the side area of the fiber, a is the radius of the curvature of the meniscus and scales with the fiber radius (see Fig. S4(a)). Since $a \sim r$ given the contact angle between the fibers and the liquid ($\theta = 20°$), hence $F_\mathrm{c} \sim \gamma h$, which agrees with the energy argument. Next, we note that the radial compression force is $F_\mathrm{r} \sim \gamma h[2\sin(\phi/2)]$, where $2\sin(\phi/2) \sim \phi$ for small ϕ (see Fig. S4(b)). Hence, $F_\mathrm{r} \sim \gamma h \phi$. As a final note, the term ϕ provides the physical intuition that the radial compression gets larger as the bundle becomes smaller, due to the effect of curvature; and the radial compression force will vanish for very small ϕ in an infinitely large bundle diameter, compared to the fiber radius.

S3.2. Elastic force within the walls of hollow bundles

Densification effects: The elastic deflection of a single soft fiber follows the linear bending moment equation $F_{\mathrm{b}}\ell \sim EI\delta/\ell^2$ under the effect of a force F_{b}, as shown in Fig. S5(a). However, to capture the behavior of the observed elastocapillary phenomena which involve densification and self-organization, we found that the simple law is not sufficient. The situation can be qualitatively different when we consider multiple hairs having spacing d, which progressively come into contact as shown in Fig. S5(b). We show the different situations of elastic deflection in Fig.S5(a) and (b) for a single fiber and a fiber array, respectively. The number of fibers is n, which is taken here to be in the tangential direction along the circumference. Applying a large enough force F_{m} leads to fiber densification by eliminating d so that the total deflection δ may be written as $\delta \sim nd$. To obtain the force law of fiber array, we sum the individual fiber deflection:

$$F_{\mathrm{m}} = \frac{EI}{\ell^2}\left[\delta + \sum_{i=1}^{n-1}(\delta - id)\right], \tag{S1}$$

Expanding Eq. (S1) yields

$$F_{\mathrm{m}} \sim \frac{EI}{\ell^2}\left[\delta n + d\frac{n(n-1)}{2}\right], \tag{S2}$$

Based on the relation $n \sim \delta/d$, Eq. (S2) becomes $F_{\mathrm{m}} \sim EI\delta^2/(d\ell^3)$ when $n \gg 1$ and using $n \sim d/\delta$. It follows a quadratic force law in the positive direction (we here consider compression only) [9, 10].

The initial configuration consists of uniformly coalesced hairs. We consider the ring shape as a stacked fiber array by virtually unfolding the structure, as illustrated in Fig. S5(c). Then, the deformation of the shrinkage of the tube is similar to the contraction of the fiber array, obeying quadratic force law, but includes fiber re-arrangement. For a single row of stacked fiber array, we can express the elastic force, $F_{\mathrm{es}} \sim EI\delta^2/(r\ell^3)$ where we replace d of F_{m} with r of F_{es} (see Fig. S5(b) and (c)). Summing the individual F_{es} of the array for which the number of rows is approximately n_{e} provides the total hoop elastic force $F_{\mathrm{e}} \sim n_{\mathrm{e}}F_{\mathrm{es}}$.

Re-arrangement effects: To express the relation of n_{e}, we derive the elastic force scaling originating from fiber re-arrangement. The total number of fibers can be written as $N \sim \rho_0 R_0 w/r^2$, where ρ_0 is the initial area fraction of fibers. Figure S6(a) shows the experimentally measured ρ_0 in various $\lambda = \ell/R_0$. Considering the geometry of ring shape (top surface of the hairy tube), the area occupied by the fibers, $A_{\mathrm{f}} \sim Nr^2$, is identical to the area of fibers occupying the ring, $A_{\mathrm{r}} \sim n_{\mathrm{e}} rR\rho_{\mathrm{f}}$, where ρ_{f} is the area fraction of fibers in the final shape. We experimentally observe that ρ_{f} is constant (see Fig. S6(b)), and we attribute this to random granular-like packing. Comparing between A_{f} and A_{r}, leads to $Nr^2 \sim n_{\mathrm{e}} rR\rho_{\mathrm{f}}$, we obtain $n_{\mathrm{e}} \sim Nr/(R\rho_{\mathrm{f}})$. Replacing N with $\rho_0 R_0 w/r^2$

and R with $R_0 - \delta$ in n_e relation yields $n_e \sim R_0 w\rho_0/[r\rho_f(R_0 - \delta)]$. Thus, F_e can be written as $F_e \sim n_e F_{es} \sim \alpha E I R_0 \delta^2/[r\ell^3(R_0 - \delta)]$, where $\alpha = \alpha_p w\rho_0/(r\rho_f)$ is the structural coefficient. We have a prefactor α_p to predict the deformation trend precisely, and $\alpha_p = 5$ in Fig. 3(d).

S4. Competition between time scales

The competition between the time scales of fiber aggregation (bundle wall thinning), τ_a, and inner diameter closure (flopping), τ, provides insights into the transition of behavior between the slow and fast drainage.

Time scale of fiber aggregation (bundle wall thinning), τ_a: The dynamics of the fiber aggregation plays an important role in the rate at which the liquid is squeezed out while the fibers are coalescing. One can imagine a wet bundle initially containing liquid between the fiber spacing, where the liquid is squeezed out during a time scale τ_a by capillary induced shrinkage (wall thinning), as shown in Fig. S7. Considering volume continuity, the aggregation speed of tube volume, $\dot{w}\ell R_0$, is the same magnitude with the drainage-induced liquid flow, $u_d w R_0$, which gives the characteristic velocity within the fiber spacing, $u_d \sim \dot{w}\ell/w$. Next, the capillary and viscous energy rate can be written as $\dot{E}_c \sim \gamma\ell\dot{w}$, and $\dot{E}_v \sim \mu u_d^2 w\ell/d$, respectively, so $u_d \sim [\dot{w}\gamma d/(\mu w)]^{1/2}$. Combining the foregoing relations, $u_d \sim \dot{w}\ell/w$, and $u_d \sim [\dot{w}\gamma d/(\mu w)]^{1/2}$, we obtain the characteristic speed of fiber aggregation $\dot{w} \sim \gamma d w/(\mu\ell^2)$. Consequently, the time scale of fiber aggregation can be scaled as $\tau_a \sim w/\dot{w} \sim \mu\ell^2/(\gamma d)$. The typical value of the aggregation time scale of water in our bundles is $\tau_a \approx 1.6$ s when $\ell = 20$ mm.

Time scale of inner diameter closure (flopping), τ: At fast drainage, the flow rate of the liquid column in the vertical direction is $Q_h \sim u R_d^2$. Considering the volume of the liquid column, $V \sim h_d R_d^2$, the time scale of the vertical drainage in the internal hole of the bundle can be expressed as $\tau_h \sim V/Q_h \sim h_d/u$. By using the relation $h_d \sim [\gamma\mu u/(\rho g d)^2]^{1/3}$, we obtain $\tau_h \sim [\gamma\mu w/(\rho g d)^2]^{1/3} u^{-2/3}$. As the inner diameter closes (flopping), a relative radial flow develops and can be expressed as $Q_f \sim \bar{u}_f A_d$, where $A_d \sim h_d R_d$ is the surface area of the internal bundle hole. Considering $V \sim h_d R_d^2$, the time scale of this closure can be scaled as $\tau_f \sim V/Q_f \sim R_d/\bar{u}_f$. The continuity $Q_f = Q_h$ leads to $\bar{u}_f \sim u R_d/h_d$, allows us to write $\tau_f \sim h_d/u \sim \tau_h$. Therefore, we can express the time scale of the closure of the bundle wall as τ without subscript: $\tau \sim [\gamma\mu w/(\rho g d)^2]^{1/3} u^{-2/3}$. The typical values of the closure time scales of water are $\tau \approx 12$ s when $u = 0.1$ mm/s for slow drainage, and $\tau \approx 0.1$ s when $u = 100$ mm/s for fast drainage.

Fiber aggregation precedes inner diameter closure at slow drain rate: $\tau_a < \tau$ where $\tau_a \approx 1.6$ s and $\tau \approx 12$ s, as shown in the top images of Fig. 2(b). However, at fast drain rate, h_d is large, and the

bundle fully closes before the fiber aggregation: $\tau < \tau_a$ where $\tau \approx 0.1$ s and $\tau_a \approx 1.6$ s, as confirmed in the experimental measurements in the bottom images of Fig. 2(b).

S5. Pressure gradient of the liquid column

At the fast drainage, we indicate the existence of two stages at high drain rate. Stage I: During the motion of the stage (see Fig. S8(a)), a tall h_d develops and the liquid column has negative capillary pressure leading to the closure of the bundle. Stage II: The motion stops and the internal pressure turns positive, additional drainage with velocity $\bar{u}_f$ takes place (see Fig. S8(b)). Our model focuses on Stage I where the negative pressure builds up along the dynamical rise height h_d, as shown in Fig. S8(a). The bundles behave very softly, so the radius of the liquid meniscus on the top of the tube, R_d, is formed obeying Jurin's law $h_d \sim \gamma/(\rho g R_d)$, and generates negative pressure along h_d. The time scale is set when the negative pressure pulls the bundle wall inward generating a relative (viscous) liquid flow in the outward direction.

S6. Dynamic structural coefficient β

Liquid drainage is strongly resisted within the fiber spacings in the bundle's wall due to the high viscous stress in the fast drainage regime. The tubes behave "softly" as individual, not as densely packed and re-arranging fiber arrays. The elastic deformation of the hairy tube follows the linear force law, $f_{es} \sim EI\delta_d/\ell^3$, so f_e is linearly proportional to δ_d of fibers with N numbers: $f_e \sim N f_{es} \sim NEI\delta_d/\ell^3$. By using $N \sim \rho_0 R_0 w/r^2$ in S2.2, we can rewrite

$$f_e \sim \beta \frac{R_0 EI}{r\ell^3}\delta_d, \tag{S3}$$

where $\beta = \beta_p w\rho_0/r$ is a dynamic structural coefficient. We have a prefactor β_p to predict the morphing behavior trend precisely. The theoretical line in Fig. 4(c) is for $\beta_p = 3.5$.

S7. Transition from partial to complete closure of hollow bundles

The foregoing scaling laws allow us to predict the transition of morphing trend between partial and complete closures. We use a dimensionless equation $\bar{R} = 1 - \Omega$, where $\Omega = \bar{\delta} + \bar{\delta}_d$ is the dimensionless total deflection. We plot R of the inset of Fig. S9 according to our scaling law to find the scattered data collapse together in Fig. S9. We vary the coefficients of Ω to fit the experimental data. The representative tube radius of our model is a mean radius between the inner and outer radii of the tubes, so the contracted radius never becomes zero even the tubes completely close. We

note that the majority of experimental data of complete closure (filled symbols) are concentrated on $\bar{R} \approx 0.2$. After complete closure of tubes, $\bar{R}$ remains constant at 0.2 despite an increase in Ω.

S8. Effect of liquid viscosity

To investigate how the properties of liquids influence on the dynamic capillary morphing, we repeat our experiments with ethylene glycol, instead of water. At slow drainage, δ will be increased as increasing γ (decreasing R), since the compression force is driven by surface tension. At fast drainage, however, δ_{d} will be increased as increasing not only γ, but also μ (behaving complete closure), since high viscous liquids increase h_{d}, leading to strong capillary compression at the hole: $f_{\mathrm{c}} \sim \gamma h_{\mathrm{d}}$. As shown in Fig. S10(a), our kinematic model appropriately describes the effects of liquid properties. Furthermore, Fig. S10(b) shows that our model still captures the morphing behavior well, even changing the liquid properties.

S9. Morphing behavior of partial/complete closure in other geometries

More complex and intriguing morphing behavior of partial/complete hole closure can be observed in other bundle geometries. We fabricate triangular bundles separated by a triangular hole, as shown in Movie S2 and Fig. S11(a). Similar to the experiments in the main text, they morph their shape in two distinct modes induced by dynamic capillarity. Next, we fabricate six triangular bundles which include three triangular holes, as shown in Movie S2 and Fig. S11(b). Using the same type of controlled experiments, we show that the dynamics dictate interesting pattern selection. The bundles can form three holes (at lowest drain rate), or collapse the holes into a closed shape (at the highest rate). We note that the hair also transforms the geometry of the internal bundle's holes at slow drain. This pattern transformation can be explained by peculiar hair re-arrangement that will go beyond the scope of the current letter. Finally, we show that the morphing of hollow bundles can be triggered by a needle inserted into the bundle instead of moving into and out of reservoir, as shown in Fig. S11(c). Please note that the drain dynamics is controlled by a syringe pump, not a linear stage. This system is useful in more practical engineering applications.

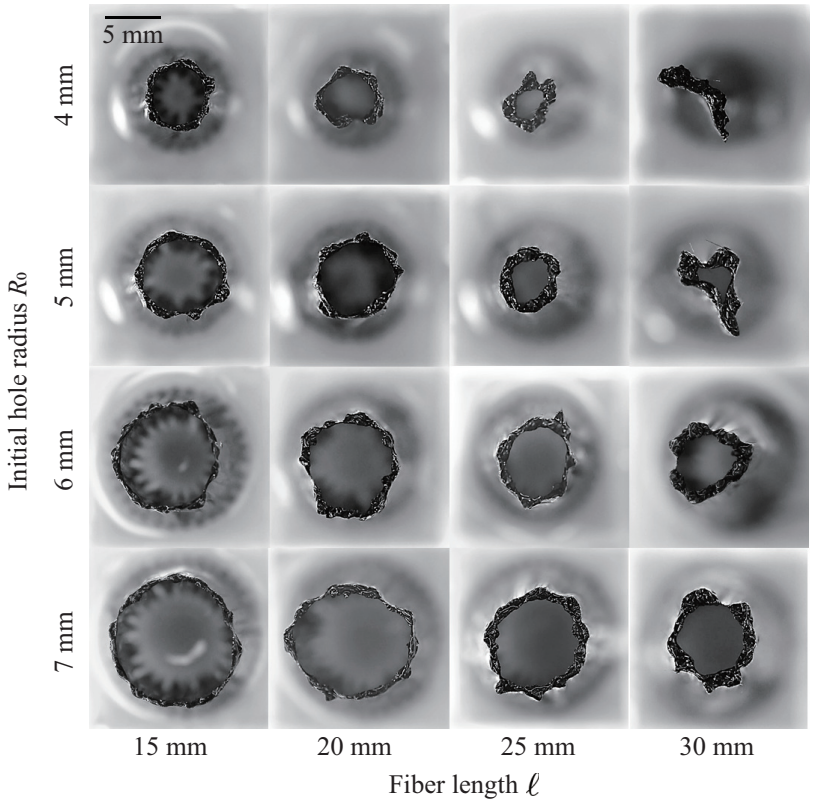

FIG. S1: The top view images of the final shape in the slow drainage (partial closure). At $R_0 \leq 5$ mm and $\ell = 30$ mm, which is the extreme cases (small R_0, long ℓ), the bundle is unstable. At the last, the tube with $R_0 = 4$ mm and $\ell = 30$ mm always collapses even at the slow drainage.

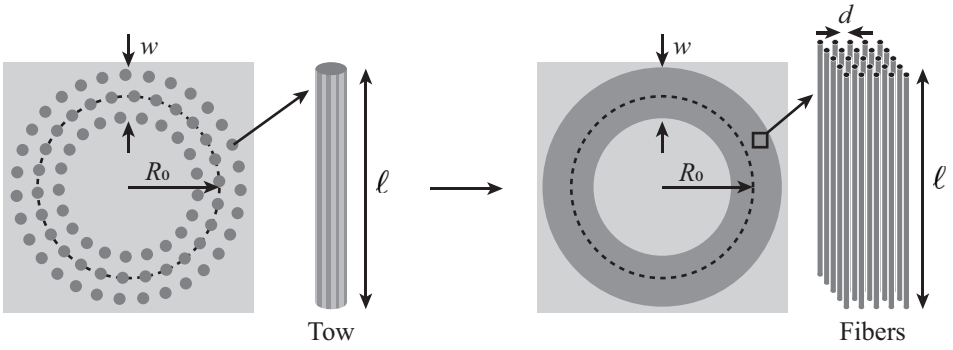

FIG. S2: Model approximation. The geometry of the hairy tube is considered from the left to the right side.

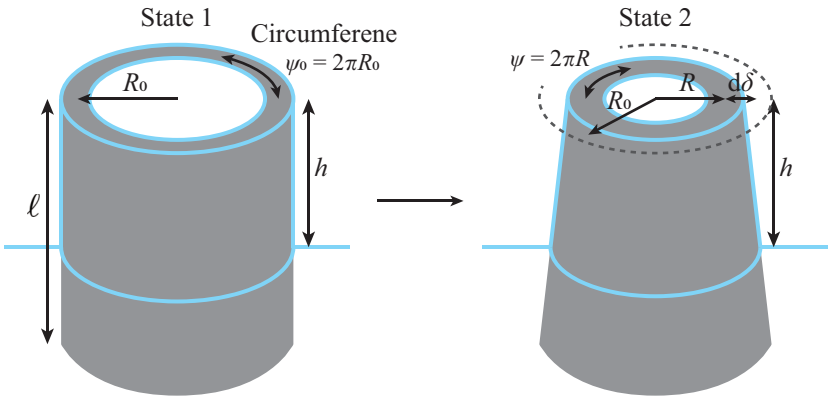

FIG. S3: The shape changes of the hairy tubes between states 1 and 2. The top area of both state 1 and 2, referred by the blue lines, is constant.

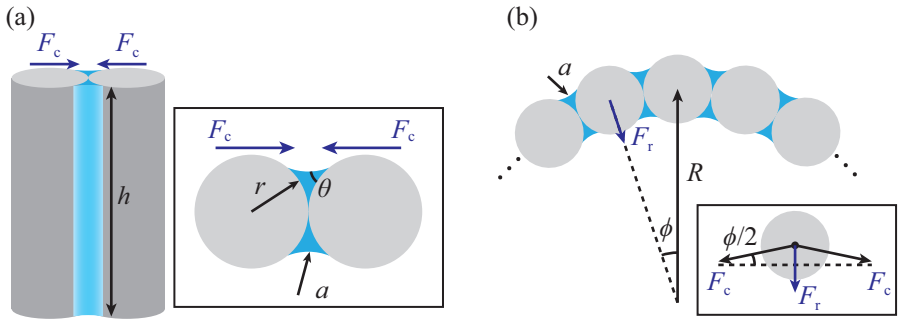

FIG. S4: Compression of fiber clusters due to capillarity. (a) Capillary force between contacting two fibers. Inset shows the top view of the liquid meniscus. (b) Force in radial direction. Inset shows free body diagram of a single fiber.

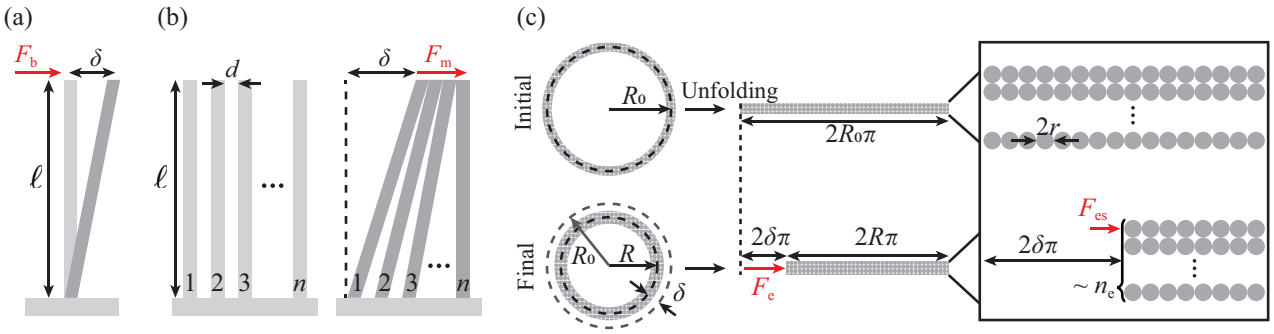

FIG. S5: Resistance of fiber clusters due to elasticity. (a) Deflection of a single fiber with radius r. (b) Deflection of multiple fibers with spacing d. (c) Schematics of nonlinear deflection of fiber array structures assembled into ring-shaped cross-section. Top and bottom images indicate initial and final configuration of hairy tubes, respectively. Black box shows close-up view of stacked fiber arrays.

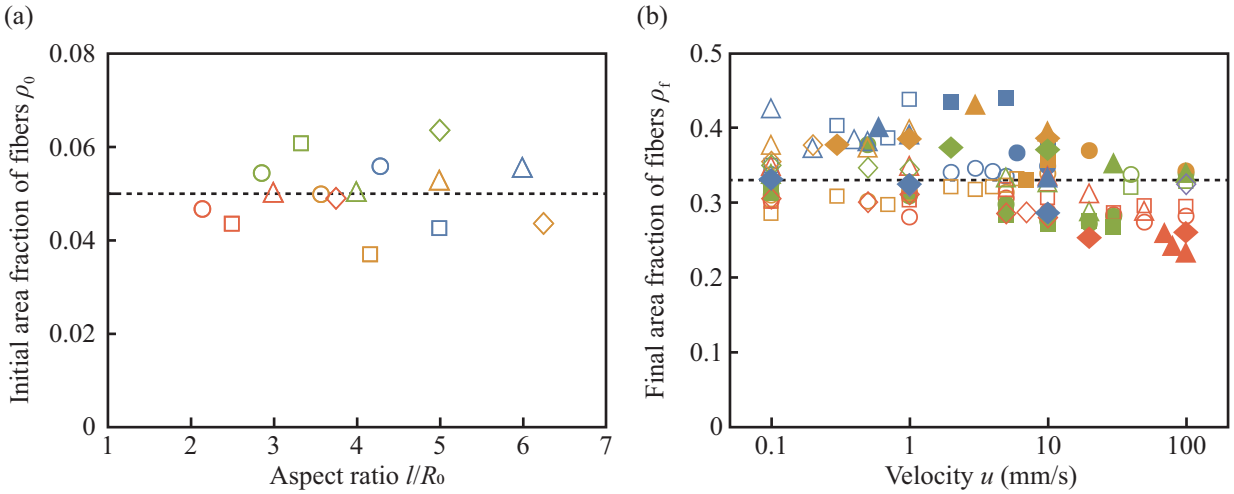

FIG. S6: The measurement of area fraction of fibers. (a) Initial area fraction ρ_0 versus aspect ratio $\lambda = \ell/R_0$. The dashed line corresponds to the average $\rho_0 = 0.05 \pm 0.01$. (b) Final area fraction of final shape ρ_f versus drain velocity u. The dashed line corresponds to the average $\rho_f = 0.33 \pm 0.05$. Empty and filled symbols correspond to the partial and complete closure, respectively. The symbols for different geometry are listed in Fig. 3(b).

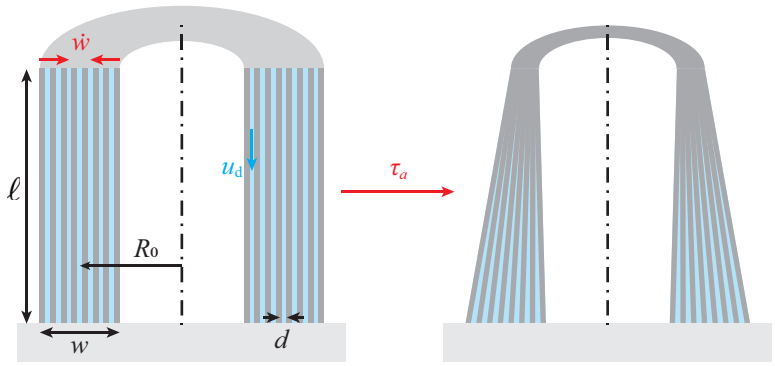

FIG. S7: Schematics of the time scale of fiber aggregation. The left and right sides of the schematics indicate the initial and final states, respectively.

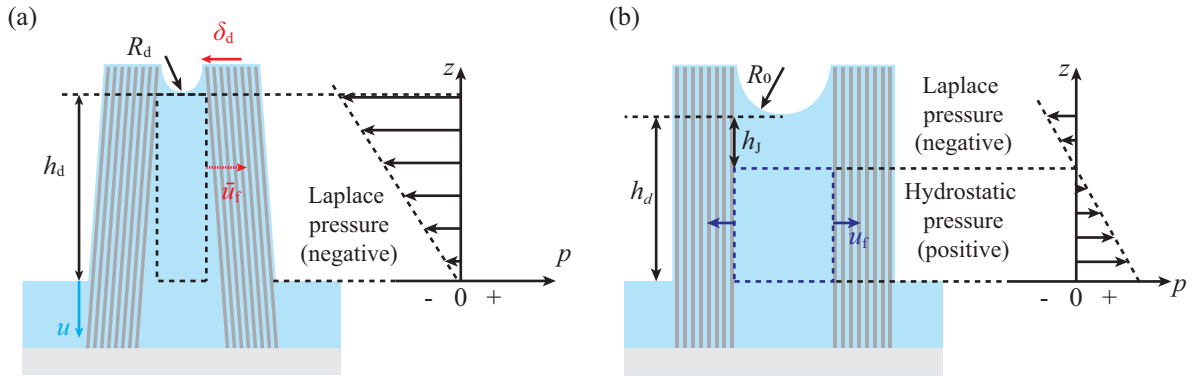

FIG. S8: The pressure gradient of the liquid column at Stage I (a) and Stage II (b).

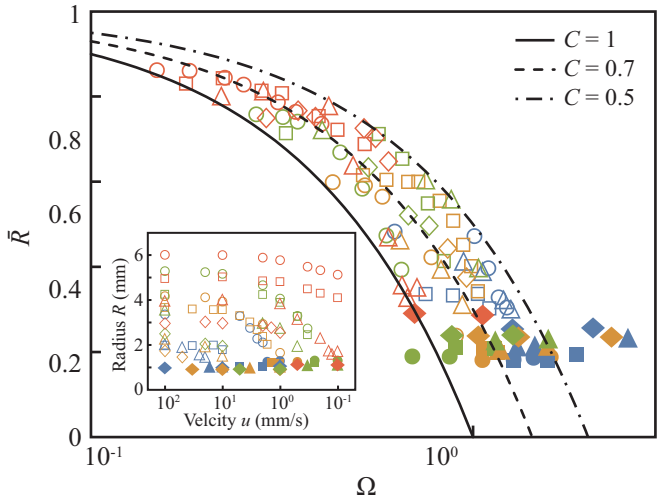

FIG. S9: Tube closure with dynamic effects. The black lines indicate theoretically predicted deflection curves $\bar{R} \sim 1 + C\Omega$ with constant $C = 1$, 0.7, and 0.5. Empty and filled symbols correspond to the partial and complete closure, respectively. Inset: Experimental data of R with respect to u. The symbols for different geometry are listed in Fig. 3(b).

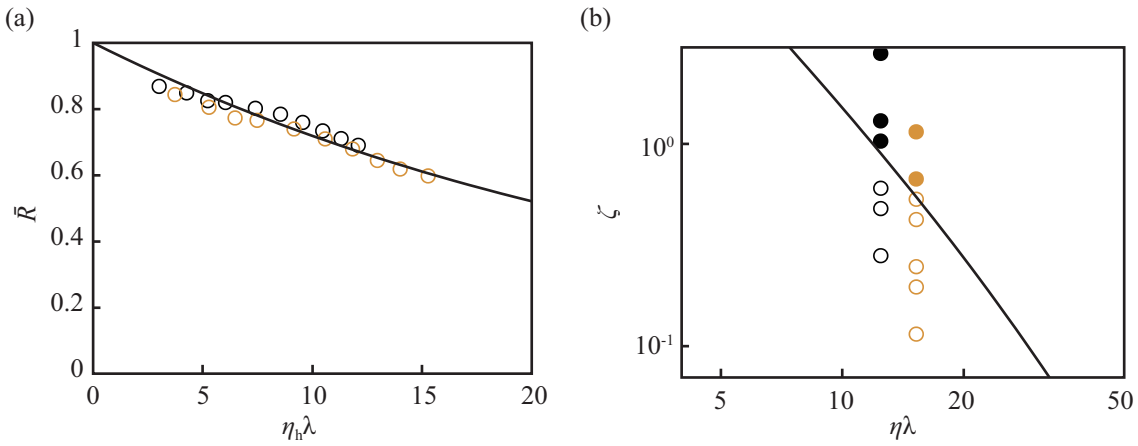

FIG. S10: Effects of liquid properties. (a) Kinematic contraction of the tube radius at slow drainage. (b) Regime map of morphing behavior. Black and orange colors correspond to ethylene glycol ($\rho = 1112$ kg/m^3, $\mu = 0.018$ Pa·s, $\gamma = 0.048$ N/m) and water ($\rho = 998$ kg/m^3, $\mu = 0.001$ Pa·s, $\gamma = 0.072$ N/m), respectively. Empty and filled symbols correspond to the partial and complete closure, respectively. The sample geometry is $R_0 = 7$ mm and $\ell = 25$ mm.

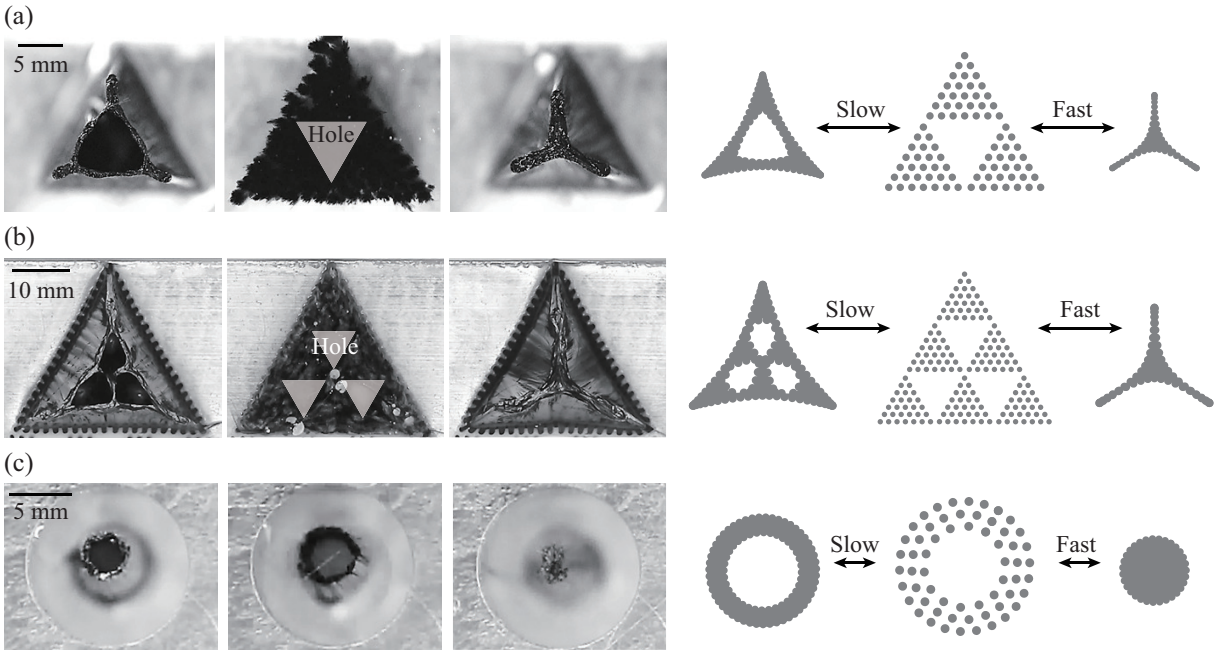

FIG. S11: Dynamic capillary morphing in more complex patterns. (a) Fractal structures with a triangular hole. The length of carbon fibers is 17 mm. Drainage velocities of the slow and fast cases are 0.6 and 60 mm/s, respectively. (b) Fractal pattern with three holes. The length of carbon fibers is 25 mm. Drainage velocities of the slow and fast cases are 10 and 310 mm/s, respectively. (c) Hollow bundles morphing using a droplet supplied by a syringe pump. The syringe pump ejects and retracts a droplet at the center of the bundle. The flow rates of the slow and fast cases are 0.1 and 3 ml/min, respectively. Left: experimental images. Right: schematics.

Movie S1. Capillary morphing of hollow bundles at slow rate followed by fast rate followed by slow rate. Tow view (left) and side view (right)

Movie S2. Capillary morphing of fractal geometry at slow rate and high rate. The video shows two experiments on different bundle geometries.